Ceramics International 52 (2026) 722–734

Contents lists available at ScienceDirect

Ceramics International

journal homepage: www.elsevier.com/locate/ceramint

Influence of infill geometry on the degradation performance of 3D printed TiO_2 photocatalytic filters

Jyoti [a,*], Marco Mariani [a], Francesca Nanni [a], Claudia Mazzuca [b], Mario Bragaglia [a]

[a] University of Rome "Tor Vergata,", Department of Enterprise Engineering "Mario Lucertini", Via del Politecnico 1, 00133, Roma, Italy
[b] University of Rome "Tor Vergata", Department of Chemical Science and Technologies, Via della Ricerca Scientifica 1, Rome, 00133, Italy

ARTICLE INFO

Keywords:
3D printing
TiO_2
Filters
Coating
Photocatalytic

ABSTRACT

In this study, TiO_2 filters with complex geometries (i.e., grid, honeycomb and gyroid) were 3D printed via direct ink writing (DIW), sintered at 1350 °C, coated using a sol-gel method and treated at 600 °C to induce the formation of anatase-phase TiO_2. The sintered TiO_2 filters exhibited a relative density between 92.19 % and 94.81 %, with shrinkage ranging from 19 % to 22 %. XRD and SEM analyses confirmed the formation of the anatase phase and a uniform coating with a thickness of 4.3–4.5 μm on the TiO_2 filters. The surface-engineered TiO_2 filters were evaluated for the photocatalytic degradation of Rhodamine B under UV light. Among the tested structures, the gyroid geometry exhibited the highest performance (completely degrading Rhodamine B in 200 min) due to its higher surface area.

1. Introduction

Titanium dioxide (TiO_2) has become one of the most extensively studied functional materials in state-of-the-art applied research. TiO_2 is an n-type semiconductor known for its impressive activity in heterogeneous photocatalysis under UV light exposure [1,2]. TiO_2 exists in three crystalline phases, with rutile and anatase being the most extensively studied. Rutile is thermodynamically and mechanically stable, making it suitable for structural applications, while anatase form stands out for exhibiting the highest efficiency in oxidation reactions [3]. Because of this, anatase-rich titanium dioxide has garnered significant attention across various applications, such as the photodegradation of pollutants in water [4,5] and air [6,7], the development of self-cleaning surfaces [8], antibacterial coatings [9], and sensor technologies.

The 3D printing of TiO_2 structures has gained significant attention in recent years due to the ability to create intricate geometries with high surface area, which is critical for photocatalytic applications. Techniques such as direct ink writing (DIW) [10,11], stereolithography (SLA)/digital light processing (DLP) [12], and fused deposition modeling (FDM) have been employed to fabricate TiO_2-based structures.

DIW is an effective technique for fabricating layer-by-layer, periodic, complex, and self-supporting three-dimensional ceramic structures that retain their geometry after both printing and sintering [13]. Recent advancements in DIW have demonstrated its capability to produce complex ceramic architectures and have successfully defined the rheological criteria required for DIW of high-solid-loading TiO_2 nanoparticles [14]. Dolganov et al. [10] explored the production of TiO2 components using DIW with optimized titania inks. The addition of oleic acid and a novel support strategy enhanced print quality, reducing cracks and warping during the drying process. Furthermore, Elkoro et al. [15] employed DIW to create monolithic structures using a low-temperature chemical sintering method. The resulting structures retained a high anatase content and exhibited excellent photocatalytic activity for the removal of gas-phase acetaldehyde. Regarding SLA, several efforts to print titania-based composites have been reported by Avila-Lopez et al. [16], Kozlov et al. [17], and Mubarak et al. [18]; however, the photocatalytic performance of these composites was not assessed. An innovative SLA-based approach was introduced by Vyatskikh et al. [19], who printed a resin containing a dissolved titanium organo-compound and subsequently pyrolyzed the resulting green part, obtaining photoactive structures. DIW, in particular, has shown great promise due to its versatility in processing ceramic materials. In this method, a TiO_2-loaded ink is extruded through a nozzle to build layer-by-layer structures, which are then sintered at nearly 1300 °C to achieve the desired mechanical strength and crystallinity [20]. The ability to tailor the ink composition and printing parameters allows for precise control over the microstructure and phase composition of the final product. However, predominantly in the rutile phase, TiO_2

* Corresponding author.
E-mail address: chaubejyoti@gmail.com (Jyoti).

https://doi.org/10.1016/j.ceramint.2025.11.372
Received 21 August 2025; Received in revised form 4 November 2025; Accepted 25 November 2025
Available online 26 November 2025

fabricated at high temperatures exhibits poor photocatalytic activity, largely due to its smaller average pore size of 13.1 nm compared to 33.8 nm in the anatase phase calcined at 700 °C. This represents a reduction of over 60 %, which significantly limits mass transport and reduces the active surface area essential for efficient photocatalysis [21]. Additionally, titanium dioxide's capacity for easy doping further expands its functionality, making it effective even under visible light illumination [22]. In practical applications, TiO_2 can be incorporated into surfaces either as thin films or as nanoparticles dispersed in composite materials. Thin films of titanium dioxide can be deposited using techniques like magnetron sputtering [23], spin coating [24], dip coating [25], pulsed laser deposition [26], and chemical vapor deposition [27]. When the target surface is titanium, anodization is a distinctive method to create a photoactive TiO_2 layer [28]. By optimizing the coating parameters, it is possible to achieve a conformal anatase layer on a rutile substrate, creating a heterojunction that facilitates efficient charge carrier separation and enhances photocatalytic activity.

The photocatalytic behavior of TiO_2 has been extensively studied for water purification applications, particularly for the degradation of organic pollutants and the inactivation of harmful microorganisms [1]. When exposed to UV light, TiO_2 generates electron-hole pairs, which react with water and oxygen to produce reactive oxygen species (ROS) such as hydroxyl radicals (OH) and superoxide anions (O_2^-). These ROS are highly effective in breaking down organic contaminants into harmless byproducts such as CO_2 and H_2O [4,5]. The efficiency of this process is highly dependent on the surface area, crystallinity, and phase composition of the TiO_2 material. For example, the presence of both rutile and anatase phases in a single structure can create a type-II heterojunction, which promotes the separation of photogenerated electrons and holes, thereby enhancing the overall photocatalytic activity.

In this investigation, TiO_2 structures with grid, honeycomb, and gyroid geometries were developed through DIW, a versatile additive manufacturing technique that allows precise control over geometry and shape. The printed samples serve as mechanically robust structures with enhanced surface area. To enhance their photocatalytic functionality, a surface modification approach was adopted through sol-gel coating using titanium tetra-isopropoxide (TTIP), followed by thermal treatment at 600 °C to induce the formation of an anatase-rich surface layer. This dual strategy leverages both the structural advantages of 3D printing and the superior photocatalytic properties of the anatase phase. The study systematically investigates the effects of printing architecture, coating uniformity, and crystalline phase development on the photocatalytic activity. Combining a 3D-printed TiO_2 filter (structure) with a conformal anatase coating, the hybrid structures were evaluated for their photocatalytic efficiency in degrading Rhodamine B (RhB) and Methylene Blue (MB), a common organic dye and model pollutant in water treatment studies. MB and RhB are chosen as model pollutants because they are widely used dyes in industries such as textiles and plastics, and are commonly found in industrial wastewater. They are toxic to aquatic life, posing significant environmental risks. Additionally, both dyes have distinct chemical properties and absorption characteristics that make them easy to detect and study during experiments on pollutant removal [29,30]. Moreover, the produced samples have been investigated with several characterizations (i.e., phase analysis, morphology, and mechanical properties).

2. Experimental

2.1. Raw materials and preliminary characterizations

The TiO_2 powder (ALTIRIS 550, HUNTSMAN, rutile phase) was provided by Huntsman. The powder exhibited an average particle size of 600 nm. Polyethylene glycol diacrylate (PEGDA, Mw 575), polyethylene glycol (PEG, Mw 400), and phenylbis (2,4,6-trimethylbenzoyl) phosphine oxide (BAPO) (C28H27O3P, Mw 418.46 g/mol) were purchased from Sigma Aldrich and used as received for the preparation of the ink. Rhodamine B (RhB, $C_{28}H_{31}ClN_2O_3$, Sigma Aldrich) and Methylene blue (MB, $C_{16}H_{18}ClN_3S$, Mw 319.85 g/mol, Fluka analytical) dye were used as the model pollutant for photocatalytic tests, which were provided by Sigma Aldrich. Ethanol (CARLO ERBA reagent) was used as a solvent. TiO_2 powder was analyzed using X-ray diffraction (XRD) and scanning electron microscopy (SEM).

2.2. Preparation of TiO_2 ink for 3D printing, rheological and chemical characterizations

The ink was prepared by mixing 70 vol% PEGDA and 30 vol% PEG as the polymeric binder. To initiate UV curing, 1 wt% of BAPO (with respect to PEGDA) was added as a photo initiator. TiO_2 powder was then added to the binder and mixed and homogenized using a planetary mixer (Thinky, AMICLAB, ARE-250, USA) at 2000 rpm for 10 min, followed by vacuum degassing to remove entrapped air bubbles. The mixture composition is 55 vol% binder and 45 vol% solid loading. The rheological properties of TiO_2-based ink have been analyzed using a rotational rheometer (KINEXUS, Malvern) equipped with a plate-plate geometry at 25 °C. The viscosity tests were performed over a 0.1 to 100 s^{-1} shear rate range at 25 °C. Fourier Transform Infrared Spectroscopy (FTIR, Agilent, Cary 630 FTIR) was conducted on the TiO_2 ink before and after UV curing. Spectra were acquired in the range of 600 to 4000 cm^{-1}.

2.3. 3D printing of TiO_2 filters

The TiO_2 ink was printed using a modified 3D printing extrusion-based system equipped with a UV light source. The ink was extruded layer by layer during printing and simultaneously cured using UV light to solidify and stabilize the printed structure, as shown in Fig. 1. The TiO_2 ink was filled into a 20 mL cartridge (Puredyne cap B5 by ViscoTec) and extruded through a nozzle with a diameter of 1.2 mm. The printing geometry designed in SolidWorks was converted into G-code using the Prusa Slicer software. The surface area values were obtained from computational estimations based on CAD geometries (SolidWorks models). This theoretical surface area was chosen as a comparative metric to evaluate the geometric potential of each infill pattern (Grid, Honeycomb, Gyroid).

Printing was carried out on a glass substrate. The process involves constructing samples layer by layer on a movable platform exposed to UV light for 60 s. The speed of the printing head has been set to 3.5 mm/s, and the layer height is 0.3 mm. The flow rate of the extrusion is 0.25 ml/min. Table 1 presents the details of the designed samples, including their notation, infill pattern type, layer height, and visual CAD models.

2.4. Thermogravimetric characterization, debinding and sintering processes

Thermogravimetric analysis (TGA, Pyris 1 TGA, PerkinElmer) was used to determine the decomposition temperature of the binder in TiO_2 ink. TGA was performed by heating 5 mg of TiO_2 green ink from room temperature to 600 °C at a rate of 10 °C/min in an air atmosphere.

The debinding process was performed in a muffle furnace (Forni De Marco, Roma) at 600 °C with a heating rate of 3 °C/min and a holding time of 120 min in an air atmosphere. Subsequently, sintering was carried out in a tube furnace (Zetasinter2-5-17TDD2, NANOE) at a temperature of 1350 °C for 3 h in air, with a heating rate of 2 °C/min.

Fig. 2 shows the TiO_2 samples before and after the sintering process. The green sample, shown before printing, represents the as-prepared ink formulation. After sintering at 1350 °C, the sample exhibited significant densification and a visible color change, indicating successful consolidation and phase transformation.

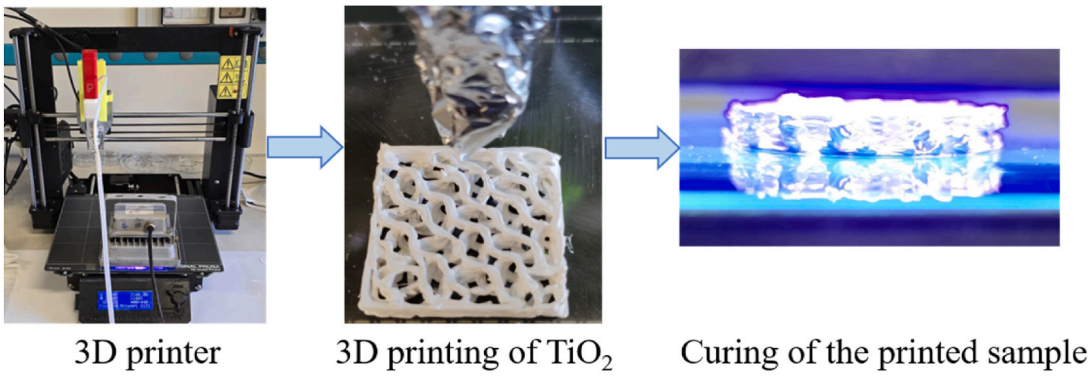

Fig. 1. Process flow image illustrating the 3D printing of the green body, followed by UV curing. (For interpretation of the references to color in this figure legend, the reader is referred to the Web version of this article.)

Table 1
Sample notations, corresponding infill patterns, infill percentage, layer height, volume of the green printed structures, CAD model images, and actual printed filter.

Sample code	Pattern	Infill %	Layer height (mm)	Volume of green printed sample (mm^3)	CAD file image	Actual printed structure
TiO_2-Gr	Grid	30	0.3	2458.16		
TiO_2-H	Honeycomb	25	0.3	2672.211		
TiO_2-Gy	Gyroid	25	0.3	2152.609		

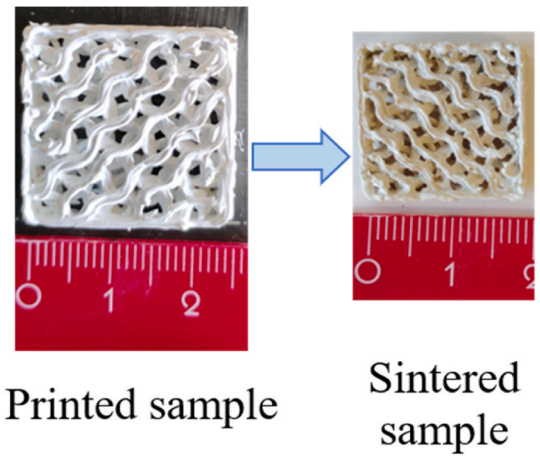

Fig. 2. Resulting TiO_2 printed samples and sintered samples after heat treatment at 1350 °C.

2.5. Physical, chemical and morphological behavior of sintered TiO_2

The density of the TiO_2 printed structure was determined by Archimedes' principle, shown in equation (1). The average density and shrinkage values were calculated based on five samples.

$$\rho = \frac{W_{dry}}{W_{dry} - W_{suspended}} (\rho w - \rho_0) + \rho_0 \quad (1)$$

Here, ρ is the density of the sample, w_{dry} is the sample's weight in air, $w_{suspended}$ is the weight of the sample when submerged in an auxiliary liquid, ρw is the density of that liquid (water), and ρ_0 is the density of air. The relative density (in percentage) was calculated by comparing the measured density of the sample (ρ) with the theoretical density of Titanium dioxide ($\rho_{TiO2} = 4.32\ g/cm^3$).

The shrinkage of the sintered ceramic samples was determined using the following formula (2):

$$\delta(\%) = \frac{(L_i - L_f)}{L_i} \times 100 \quad (2)$$

where δ represents the percentage of shrinkage, L_i is the original dimension of the sample before sintering (in mm), and L_f is the final dimension after sintering (in mm).

The crystalline phases of the sintered TiO_2 samples were identified using an X-ray diffractometer (XRD, Philips X'Pert with Ni-filtered Cu Kα radiation (λ = 1.5405 Å). Patterns were acquired in the 20–90° range with a step size of 0.02°. Scherrer's equation (3) was used to estimate the crystalline sizes of TiO_2:

$$T = \frac{K\lambda}{(\beta \cos \theta)} \quad (3)$$

Where T represents the mean crystallite size in the direction perpendicular to the examined lattice planes, K is the Scherrer constant (typically ~0.9), λ is the wavelength of the X-rays used (in nm), β is the full width at half maximum (FWHM) of the diffraction peak in radians after correcting for instrumental broadening, and θ is the Bragg angle of the

diffraction peak. A universal testing machine (Instron 5569, Techno System) with a compression fixture was employed to test the samples according to ASTM C1424-15.

Sintered TiO_2 samples, embedded in epoxy resin, have been ground using SiC papers (P400-P1200), followed by polishing with diamond suspensions and final polishing with 0.05 μm colloidal alumina. After each step, samples were cleaned with ethanol and dried with compressed air to ensure a deformation-free, polished surface for characterization. The hardness of the sample was determined using a Vickers hardness tester (Microhardness tester, FM-700), with a load of 500 g applied for 30 s. The microstructure of the sintered 3D-printed TiO2 filter was examined using a field-emission scanning electron microscope (SEM, Nano Eye, SNE-ALPHA) at an accelerating voltage of 5 kV with a secondary electron detector. Prior to SEM analysis, the samples were coated with platinum for 30 s using a vacuum coater (MSM-100P Ion Sputter Coater) and then mounted on a metal platform using conductive tape.

2.6. Surface coating with anatase sol-gel

The rutile TiO_2 3D-printed filter was coated with an anatase coating. The TiO_2 films were deposited via a sol-gel process, beginning with the preparation of the sol solution containing 3 ml of titanium tetra isopropoxide ($C_{12}H_{28}O_4Ti$, TTIP, Mw: 284.22 g/mol Sigma ALDRICH) dissolved in 50 ml of ethanol under stirring at 200 rpm for 2 h. Then, 3 ml of acetic acid (CARLO ERBA reagent) was added to catalyze the gel reaction. The TiO_2 printed structure was then immersed in the solution for 5 min before being withdrawn at a controlled speed of 4 cm/min to form a uniform wet layer. After deposition, the coated samples were left at room temperature for 14 h to allow solvent evaporation and aging, forming a solid film. The samples were thermally treated in a furnace at 500 °C with a heating rate of 3 °C/min for 2 h to obtain a dense anatase film. All samples were coated twice under the same conditions to make a homogeneous and thick TiO_2 coating on the sample. A schematic diagram illustrating the 3D printing and coating process for TiO_2 is presented in Fig. 3.

2.7. Anatase-coated filters characterization

X-ray diffraction (XRD) analysis was performed on the thermally treated sol-gel powder and sol-gel-coated filter to examine their phase composition. The microstructure of the 3D-printed TiO_2 filter after coating was characterized using field emission scanning electron microscopy (SEM).

The photocatalytic performance of the 3D-printed TiO_2 structures with surface-anatase coating was evaluated by measuring the degradation of RhB and MB under UV irradiation.

For each test, 20 mL of dye solution (initial concentration: 12 mg/L) was prepared in a clean glass beaker, and the printed TiO_2 sample was placed at the surface of the solution under continuous magnetic stirring to ensure uniform dispersion. This initial concentration simulates a more realistic, high-loading pollutant scenario, allowing for robust evaluation of the filter capacity over a fixed period.

Photocatalytic degradation was initiated using a UV-A LED source (Philips UV, 40 W, $\lambda = 350$ nm), and the reaction progress was monitored at regular time intervals.

RhB was selected as the model pollutant to analyze the degradation kinetics in detail. At predetermined time intervals (0, 10, 20, 30, 60, 90, 120, 180, 240, 300, and 330 min), 1 mL aliquots were extracted and immediately diluted with 2 mL of deionized water to maintain the absorbance within the linear range of the UV–Visible spectrophotometer (CARY 100 Scan, UV–Visible spectrophotometer). The concentration of RhB was determined by measuring its absorbance at the maximum wavelength ($\lambda_{max} = 553.5$ nm). The degradation efficiency (η) under UV light was calculated using the following equation (4):

$$\text{Degradation efficiency } \eta(\%) = \frac{(C_o - C)}{C_o} \times 100 \quad (4)$$

Where C_O is the initial concentration and C is the concentration (mg/l) after UV irradiation at different time intervals. The photocatalytic performance of TiO_2 in 3D-printed structures is strongly governed by their geometry, which influences light distribution, surface area, and reactant-catalyst interaction. The degradation kinetics were analyzed using the Beer-Lambert law, and the dye concentration at each time point was calculated accordingly. Assuming pseudo-first-order reaction kinetics derived from the Langmuir-Hinshelwood (L-H) kinetic model,

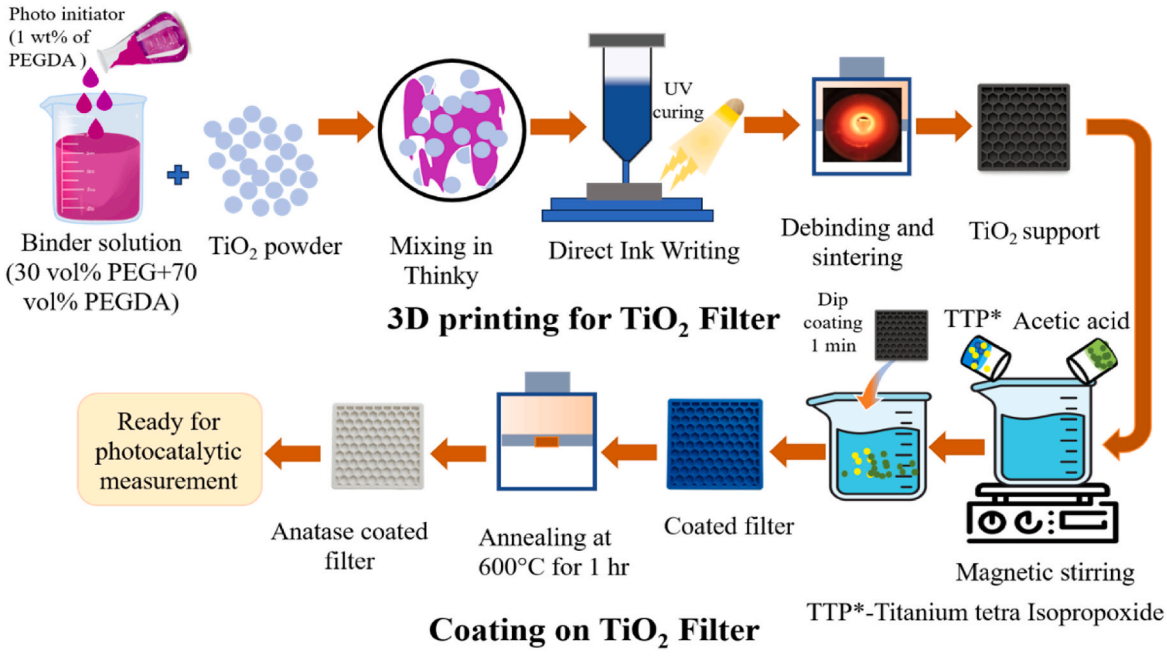

Fig. 3. Schematic illustration of the DLP 3D printing process and subsequent TiO_2 coating on the printed structure.

which is typical for photocatalytic degradation of organic dyes [31], the apparent rate constant (k) was calculated using the following equation. (5):

$$C = C_O e^{-kt}$$

$$\frac{C}{C_o} = kt \quad (5)$$

where C_o and C represent the dye concentrations at the initial time and at time *t*, respectively.

3. Result and discussion

3.1. Rheological behavior of TiO_2 ink

The rheological behavior of the TiO_2-based ink shown in Fig. 4 (a) was investigated to assess its suitability for DIW. The TiO_2 ink exhibits non-Newtonian, shear-thinning behavior, as evidenced by the decreasing viscosity with increasing shear rate in the low to moderate range, approximately up to 50 s^{-1}. At higher shear rates (above 50 s^{-1}), the viscosity decreases and begins to level off, which can be attributed to the polymeric behavior of TiO_2 in the presence of 55 vol% binder (PEG and PEGDA). This behavior likely arises from enhanced particle interactions and transient agglomeration under stronger shear forces, consistent with findings reported in previous studies on polymer-modified suspensions [32–34].

Similarly, as illustrated in the shear stress vs. shear rate graph in Fig. 4 (b), the TiO_2-based ink reveals a distinct non-linear trend characteristic of shear-thinning (pseudo-plastic) behavior. In this system, shear stress increases with increasing shear rate, indicating the presence of an initial yield stress (approximately 150–200 Pa), which is crucial for DIW inks to prevent flow under their own weight after printing. The shear-thinning nature of the TiO_2 paste enables smooth extrusion with minimal applied force, while also ensuring structural integrity post-deposition by preventing sagging, spreading, or collapse [35].

To quantify the flow characteristics or pseudo plastic behaviour, the Power Law model as expressed in equation (6)

$$\sigma = K\dot{\gamma}^n \quad (6)$$

where σ is the shear stress and γ is the shear rate, k is the consistency index, and n is the flow behavior index. This expression can also be reformulated in terms of apparent viscosity (η) as a function of shear rate in equation (7):

$$\eta = K\gamma^{n-1} \quad (7)$$

From the fitting, the flow index was determined as n = 0.003 (based on $n - 1 = -0.997$), with a coefficient of determination of $R^2 = 0.968$, indicating a strong correlation with the power model. The value of n reflects the degree of shear-thinning; specifically, $n < 1$ indicates pseudo-plastic or shear-thinning behavior. A lower n value corresponds to more pronounced shear-thinning. The extremely low n value confirms a strong shear-thinning behavior, which is essential for DIW applications where the material must flow easily through the nozzle and quickly regain viscosity to retain its shape post-extrusion [36].

This rheological profile confirms that the TiO_2-PEGDA-PEG paste exhibits pronounced thixotropic behavior: it flows easily under shear during extrusion and rapidly rebuilds structure at rest. Such characteristics make it highly suitable for DIW, where materials must exhibit both extrudability and shape retention post-deposition [35].

3.2. Thermal and chemical analysis of the ink

Thermogravimetric analysis (TGA) was conducted to evaluate the thermal decomposition behavior of the TiO_2 ink and to determine the optimal debinding and sintering conditions for the 3D-printed green sample. As shown in Fig. 5(a), the TGA curve indicates a three-stage thermal decomposition process, corresponding to the removal of different components present in the ink. The initial weight loss, observed below approximately 180 °C, was attributed to the evaporation of adsorbed water and residual solvents [37].

This stage typically represents around 2–5 % of the total mass loss. The main decomposition occurs in the second stage, between 180 °C and 400 °C, where a significant weight reduction of roughly 25 % is observed, decreasing the total mass from approximately 98 % to 73 %. Multiple peaks in the DTG curve characterize this stage. A sharp peak appears around 200–220 °C, corresponding to the rapid decomposition of PEG, which is known to degrade within the range of 180–250 °C [38]. Several smaller peaks or shoulders appear between 220 °C and 350 °C, indicating the stepwise degradation of PEGDA, which contains acrylate functional groups that decompose at slightly higher temperatures. The maximum rate of weight loss is seen around 325–350 °C, marking the peak of binder burnout. In the final stage, from 400 °C to 600 °C, the material exhibits minimal further weight loss (around 2–3 %), and the TG curve approaches a plateau. The DTG curve returns to baseline, indicating the completion of organic degradation. At this point, the residual weight is approximately 70 % of the initial mass, representing the thermally stable inorganic TiO_2 content.

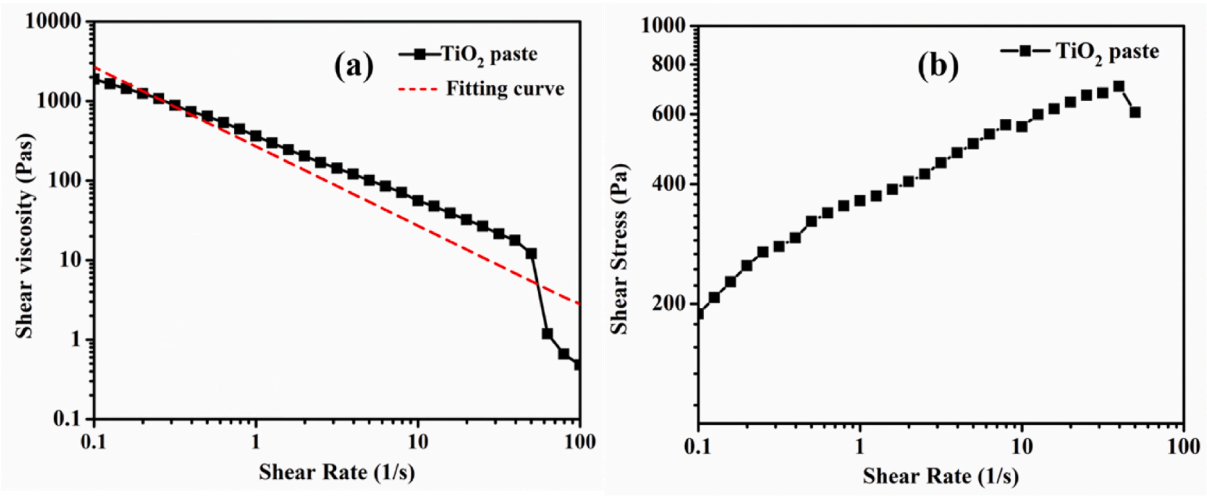

Fig. 4. Rheological behavior of the TiO_2-based ink: shear-thinning behavior (a) shear viscosity vs shear rate, (b) shear stress vs shear rate.

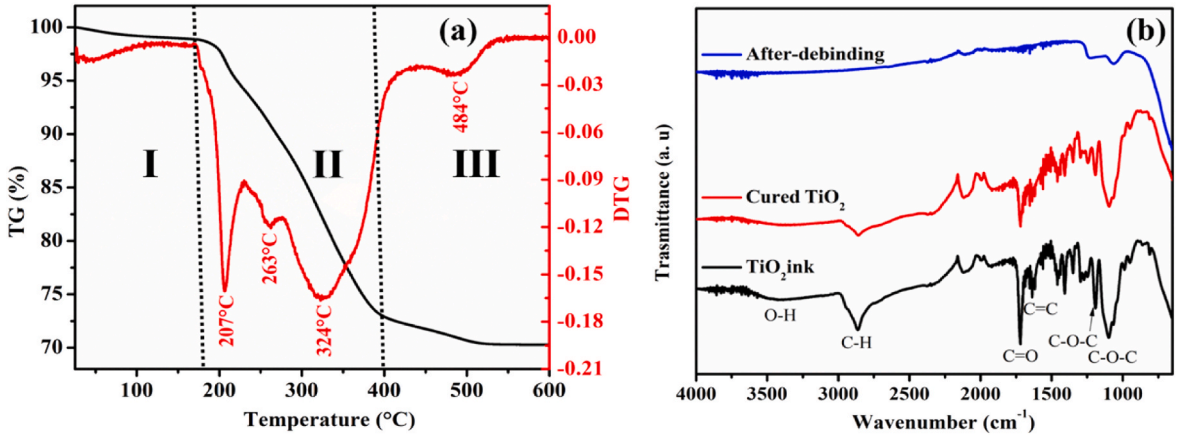

Fig. 5. (a)Thermogravimetric analysis (TGA) of the TiO_2 ink, (b) FTIR spectrum of TiO_2 ink before and after curing, and debinding.

Overall, the total weight loss of 30 % corresponds to the removal of the organic binder system. A gradual heating profile, particularly between 180 °C and 400 °C, would enable efficient removal of binders. These thermal characteristics are essential for optimizing the debinding and sintering process of 3D-printed TiO_2 structures. The FTIR analysis of TiO_2 ink containing PEG and PEGDA binders reveals evolving spectral features during curing and debinding, as shown in Fig. 5(b), reflecting chemical and structural changes.

Before curing, the ink exhibits distinct organic peaks. PEG contributes strong C-O-C stretching near 1100-1110 cm^{-1} (ether bonds), C-H stretching at 2870-2940 cm^{-1} (alkyl groups), and a broad O-H peak around 3300-3500 cm^{-1} (hydroxyl groups or moisture). PEGDA adds a sharp C=C stretch at 1630-1650 cm^{-1} (acrylate double bonds) and a C=O signal near 1720 cm^{-1} (ester carbonyl). TiO_2 appears as a broad Ti-O-Ti vibration below 700 cm^{-1}, with slight shifts in PEG's C-O-C peak due to hydrogen bonding with TiO_2 particles [39]. After UV curing, the C=C peak (1630–1650 cm^{-1}) diminishes, confirming PEGDA cross-linking via acrylate polymerization. PEG's C-O-C and C-H peaks persist, indicating stability, while the O-H band may weaken if curing reduces moisture. Ti-O-Ti vibrations of TiO_2 intensify as in the previous one.

Following debinding, organic signatures (C-O-C, C-H, C=O) disappear, confirming binder removal via thermal decomposition. The spectrum becomes dominated by Ti-O-Ti vibrations below 700 cm^{-1}. Weak residual peaks near 1450 cm^{-1} may indicate trace carbonates from carbonized organics [40,41].

3.3. Density, shrinkage and mechanical properties of the sintered TiO_2

Sintering was performed at 1350 °C to achieve densification of the 3D printed TiO_2 ceramic structures. The bulk density of the sintered TiO_2 samples ranged from 3.9 to 4.01 g/cm^3, corresponding to a relative density between 92.19 % and 94.81 %. These results indicate that the sintering process achieved substantial densification, with only minimal residual (closed) porosity remaining in the printed structures. The volumetric shrinkage of the sintered grid patterns, honeycomb, gyroids, and bar-shaped samples ranged from 48 % to 55.9 % depending on the sample geometry. This variation in shrinkage can be attributed to differences in internal architecture, packing density, and the surface area-to-volume ratio of each design. Open structures, such as gyroid and grid patterns, often exhibit slightly higher shrinkage due to more available free volume and differential densification behavior during sintering [42]. In the context of ceramic additive manufacturing, especially with DIW, controlling both density and shrinkage is critical to ensure dimensional accuracy and mechanical reliability. Table 2 summarizes key physical and dimensional characteristics of the printed samples. It includes measured density, relative density, directional and volumetric shrinkage, calculated theoretical surface area, and images of the actual printed structures. The specific surface area of the different filter

Table 2
Density, shrinkage percentages, surface area, and actual printed structures of the samples.

Sample	Density g/cm^3	Relative density (%)	Shrinkage X (%)	Shrinkage Y (%)	Shrinkage Z (%)	Volumetric Shrinkage (%)	Surface area (mm^2)	Actual printed structure
TiO_2-Gr	3.971	93.87	20.14	19.77	21.22	49.53	1449.2	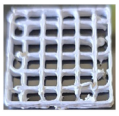
TiO_2-H	3.93	92.92	19.86	19.25	20.47	48.54	1526.87	
TiO_2-Gy	3.9	92.19	19.58	19.41	20.52	48.53	1696.046	
TiO_2-Bar	4.01	94.81	22.36	18.92	21.31	50.47	–	

geometries was calculated using geometric CAD models using SolidWorks software (Dassault Systèmes). These parameters help evaluate print accuracy, material densification, and dimensional changes that occur after processing.

At 1350 °C, density reaches approximately 92.19–94.81 % of the theoretical value. This aligns with literature reports: conventional cold compaction achieves ~86 % density after sintering at 1350 °C [43], while 3D-printed TiO_2 samples sintered at the same temperature attain ~95 % density [44]. The sintering temperature is a critical factor influencing the density of TiO2 ceramics through diffusion-controlled densification and grain growth. While higher temperature generally improves density, exceeding system-specific thresholds causes microstructural degradation. Optimal temperatures balance densification with phase stability, with dopants enabling high density at reduced temperatures for energy-efficient processing [45,46].

Although the primary focus of this study is the photocatalytic performance of TiO_2, mechanical characterization was also performed to evaluate the potential of the printed structures for dual-function applications, particularly in filtration and environmental remediation systems. In such applications, the material must possess high surface activity, sufficient mechanical strength, and durability to function as a self-supporting and long-lasting component.

The compressive stress-strain behavior of the sintered dense TiO_2 sample is presented in Fig. 6. The calculated Young's modulus was approximately 5.5 GPa, reflecting the inherent stiffness of the printed ceramic structure. The maximum compressive strength reached 146 MPa, demonstrating the robustness of the sintered component. These mechanical properties are consistent with previous studies, such as Chen et al. [20], that reported an elastic modulus of up to 6.87 GPa and a compressive strength of 125 MPa for DIW-printed TiO_2 ceramics sintered at 1300 °C. Similarly, Aleni et al. [47] documented TiO_2 samples with elastic modulus values around 5 GPa and compressive strengths of approximately 100 MPa. The alignment of our results with the literature confirms the reliability and effectiveness of the DIW process for fabricating high-strength TiO_2-based ceramics.

In addition to compressive performance, the Vickers hardness of the 3D-printed TiO_2 sample was measured to be 917 HV (equivalent to 8.99 GPa), which is in close agreement with the values reported by Caravaca-Kosteski et al. [48], who measured the hardness of rutile TiO_2 to be 8.6 GPa (fail model) and 12.28 GPa (fracture model) using conventional sintering methods. The relatively high hardness can be attributed to the fine microstructure resulting from the layer-by-layer deposition, high relative density achieved through optimized sintering, and the presence of a dominant rutile phase, which is mechanically stronger than anatase [46]. This is particularly relevant for applications where photocatalytic structures may be exposed to mechanical stresses during handling, installation, or operation under flowing fluids.

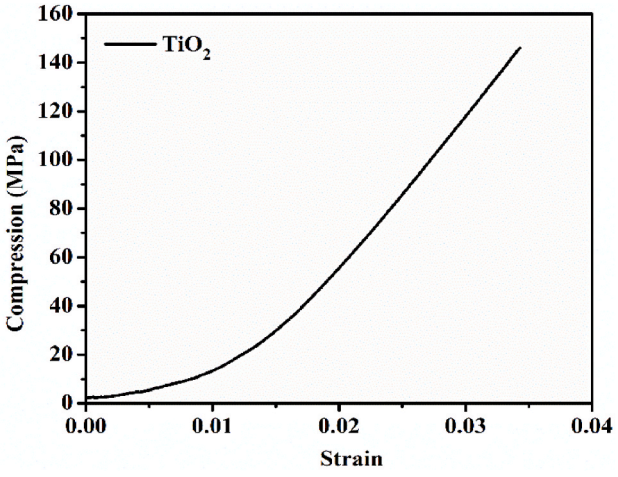

Fig. 6. Compressive stress versus strain responses measured for a dense 3D printed sample.

3.4. Phase and microstructure analysis of sintered anatase TiO_2-coated sample

Fig. 7 presents the XRD patterns of TiO_2 samples subjected to different treatments: sintering at 1350 °C, in situ synthesis of the anatase phase at 600 °C, and coating followed by annealing at 600 °C.

The sample, sintered at 1350 °C, exhibits a pure rutile phase, as confirmed by matching with the JCPDS reference pattern (98-001-7812). The characteristic 2θ peaks for rutile are observed at 27.3988°, 36.009°, 39.1359°, 41.1598°, 43.950, 54.2958°, 56.5890°, 62.6363°, 63.9954°, 68.9326°, 69.6700°, and 76. 5094°. The same reflections were found for the raw TiO_2 powder, as shown in Fig. S1. In contrast, the XRD pattern of the in situ synthesized TiO_2 sample, prepared at 600 °C using TTIP as the precursor, confirmed the formation of the anatase phase. The anatase reflections, consistent with JCPDS 98-001-1629, appeared at 2θ values of 25.48°, 37.11°, 38.66°, 48.21°, 54.03°, 55.27°, 62.84°, 68.88°, 70.46°, 75.18°, and 76.29°. The XRD pattern of the coated and annealed sample reveals the coexistence of both anatase and rutile phases. The dominant anatase peaks are observed at 25.2° and 48.0152°. The average crystallite sizes of the sintered TiO_2 samples before and after coating are 55.4 nm and 74.1 nm, respectively. The increase in crystallite size after coating can be attributed to the crystallization and grain growth induced during the heat treatment [49]. Also, during high-temperature sintering, the coating can promote atomic diffusion at the TiO_2 grain boundaries. This enhanced diffusion accelerates the Ostwald ripening mechanism, where smaller crystallites dissolve and redeposit on larger ones, increasing average crystallite size [50]. The crystalline size of the anatase phase synthesized at 600 °C is 47.1 nm. Anatase has lower thermal stability and transforms to rutile above 600 °C; the observed size reflects the early stage of this transformation before full grain growth [51]. Rietveld refinement analysis of the coated sample indicates a phase composition of approximately 11 % anatase and 89 % rutile. Table 3 summarizes the crystallographic and physical properties of the TiO_2. The lattice parameters (a, b, c) and unit cell volumes confirm the distinct crystal structures of the anatase and rutile phases.

Fig. 8 (a) presents the fractured cross-sectional surface of the sintered TiO_2 sample. The image provides clear evidence of the layer-by-layer structure resulting from the DIW process used for fabricating the base structure of the TiO_2 filter. Notably, the printed layers are distinctly

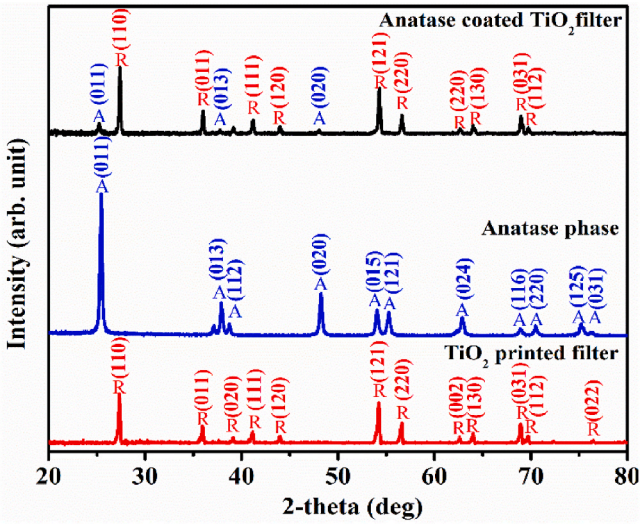

Fig. 7. XRD patterns of TiO_2 samples: rutile-phase sintered filter at 1350 °C, anatase-phase powder at 700 °C, and anatase-coated filter at 700 °C.

Table 3
Lattice parameters, unit cell volume, density, and average crystallite size of TiO_2 samples derived from XRD analysis.

Sample	a (Å)	b (Å)	c (Å)	Volume cell (Å)	Density (g/cm^3)	Average Crystaline Size (nm)
TiO_2-Rutile sintered sample-1350 °C	4.6	4.6	2.9	62.7	4.23	55.4
Anatase phase powder-600 °C	3.8	3.8	9.5	135.2	3.92	47.1

visible, highlighting the fidelity of the printing and sintering processes in preserving the designed geometry. The thickness of an individual printed layer is approximately 200–220 μm, which aligns well with the layer height during printing and the expected shrinkage behavior upon sintering.

Fig. 8 (b) illustrates the microstructure and surface morphology of the TiO_2 ceramic after sintering. Fig. 8(c) presents a magnified image of the TiO_2 sample, allowing for the determination of the grain size, which ranges from 1.0 to 1.2 μm, in accordance with the starting particle size of the raw TiO_2 powder, as shown in Supplementary Fig. S2, which ranges from 500 to 700 nm. The increase in grain size after sintering can be attributed to grain growth at high temperature (1350 °C). During sintering, atomic diffusion is significantly enhanced, leading to neck formation and grain boundary migration. These processes collectively promote densification and coarsening of grains [48].

The EDS analysis of the TiO_2 substrate provided in Fig. 8 (d) confirms the elemental composition of the filter substrate being the detected elements only titanium (Ti) and oxygen (O).

The average thickness of the anatase TiO_2 coating was estimated using SEM techniques, as illustrated in Fig. 9(a) and (b). The microstructural analysis of cross-sectional images indicates that the coating thickness ranges between approximately 4.3 and 4.5 μm. The coating was uniformly adhered to the surface of the sintered TiO_2 filter substrate, demonstrating good interfacial bonding. The adherence of the anatase coating to this structured surface further demonstrates compatibility between the sol-gel-derived film and the sintered TiO_2 substrate.

Elemental mapping by SEM-EDS (Fig. 9(c)) confirms the presence of a uniform TiO_2 coating layer, as evidenced by the detected elements titanium (Ti) and oxygen (O). The anatase TiO_2 layer was deposited via a sol-gel process, which enabled the formation of a dense and conformal coating over the TiO_2 filter substrate. The thickness of the base filter material had been predetermined and was kept consistent across all samples to ensure accurate assessment of the coating layer. As confirmed by XRD, SEM, and EDS analysis, the sol-gel route allowed precise control over the coating morphology and phase composition, resulting in a homogeneous anatase TiO_2 phase distribution.

3.5. *Photocatalytic activity of TiO_2 filters*

The photocatalytic performance of the TiO_2 filter was evaluated by studying the degradation of Rhodamine B and methylene blue under UV light irradiation, as shown in Fig. 10. The complete degradation of both dyes after 6 h of exposure demonstrates the effectiveness and versatility of the TiO_2 filter across different dye pollutants.

To evaluate the influence of structural design on photocatalytic performance, the different 3D-printed structures of grid, honeycomb, and gyroid were tested under UV light exposure in a 12 mg/l RhB solution at pH 7, and their degradation efficiencies were evaluated over time, as shown in Fig. 11(a)–(c).

The grid filter demonstrated a complete 99 % degradation of RhB in

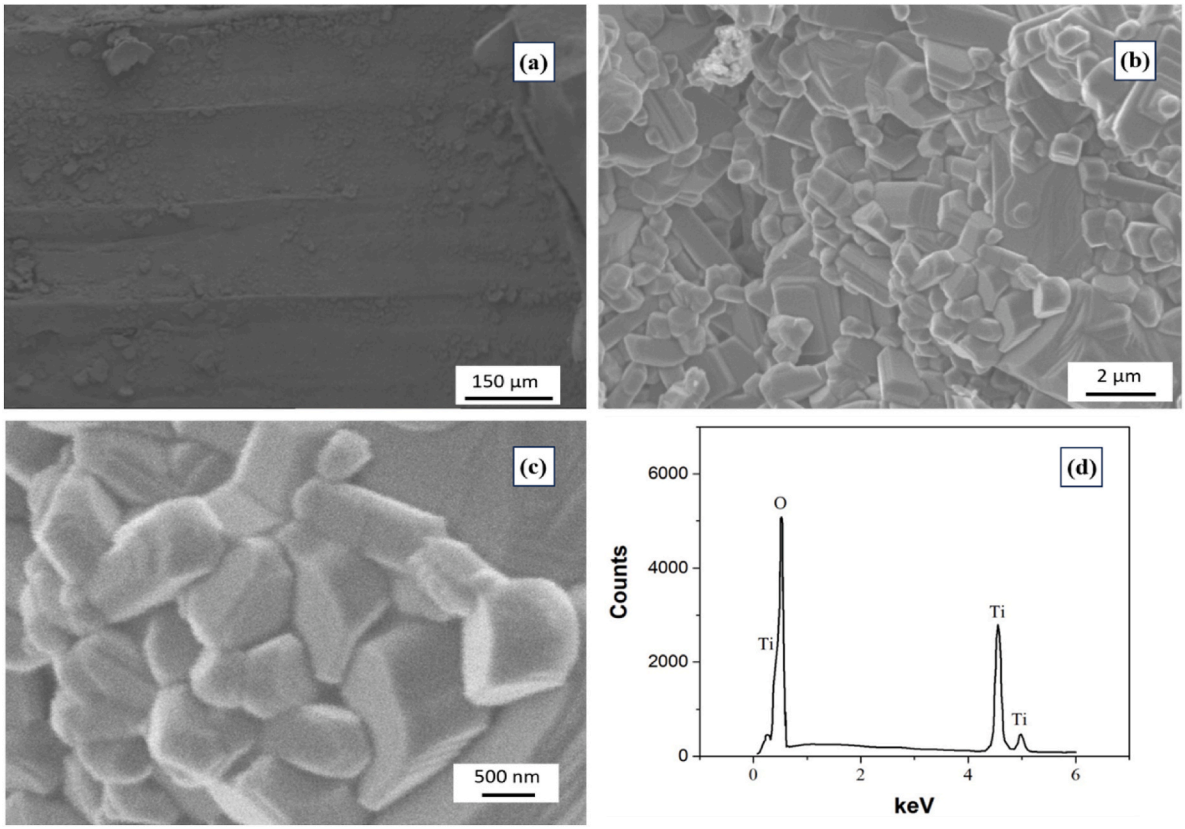

Fig. 8. (a) Printed layer thickness of the TiO_2 filter, (b) grain size of the TiO_2 sample after sintering, showing microstructure, (c) high magnification of the TiO_2 grains, and (d) EDS spectrum of the TiO_2 filter substrate.

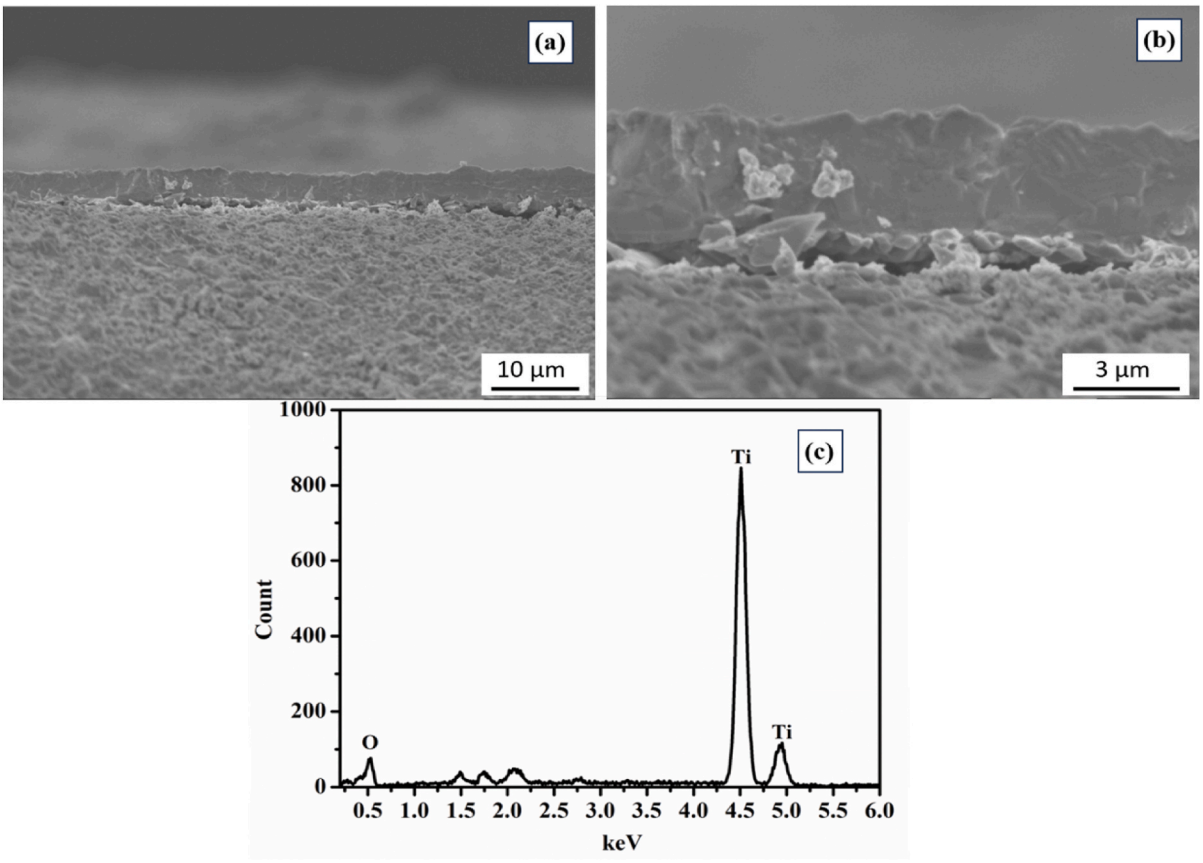

Fig. 9. (a) Cross-sectional thickness and microstructural analysis of the TiO_2-coated sample, (b) magnified image of the TiO_2-coated surface, and (c) EDS spectrum of the anatase coating.

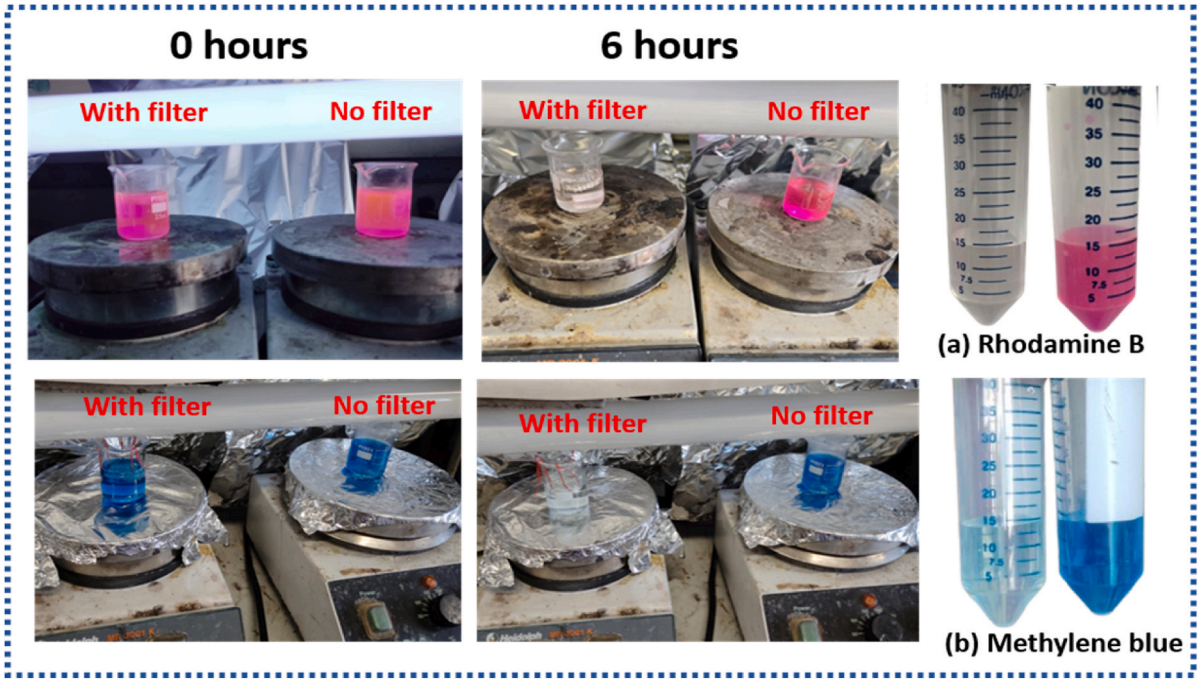

Fig. 10. Photocatalytic degradation of (a) Rhodamine B and (b) Methylene Blue after 0 and 6 h of UV irradiation, including photolysis controls without TiO_2 filters. (For interpretation of the references to color in this figure legend, the reader is referred to the Web version of this article.)

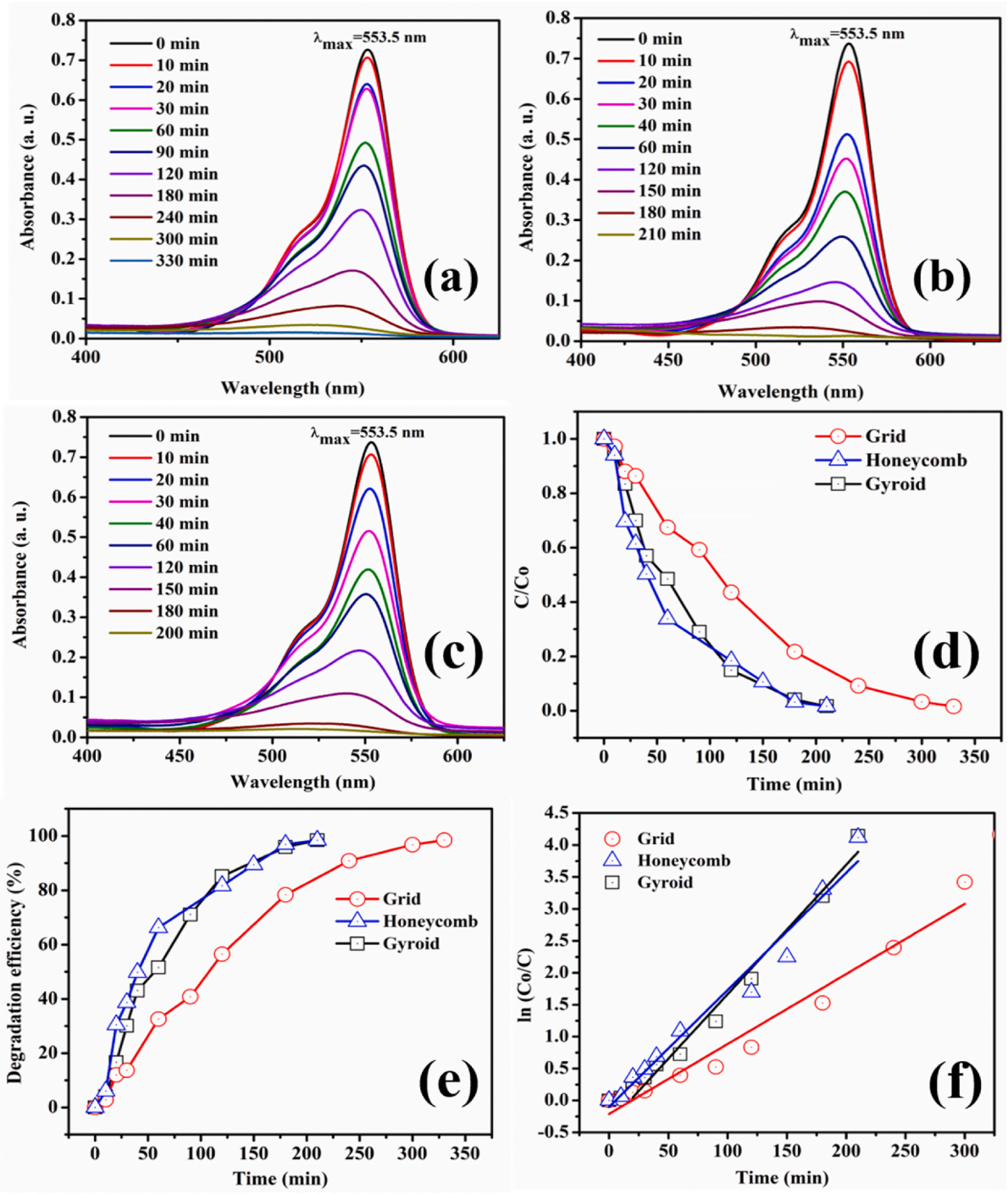

Fig. 11. (a) Grid, (b) Honeycomb, and (c) Gyroid filter photocatalytic evaluation, (d) Time-dependent photocatalytic degradation, (e) Degradation efficiency (%) after fixed irradiation time, (f) Degradation kinetics plots at different times.

UV exposure time of 330 min, as indicated by the gradual reduction in absorbance at 553.5 nm. The calculated pseudo-first-order rate constant (k) was 0.0077 ± 0.0004 min^{-1} with a correlation coefficient (R^2) of 0.986, suggesting a reliable kinetic fit. The relatively slow photocatalytic activity can be attributed to the grid's linear architecture, which offers a lower surface area, limiting the number of active sites available for dye degradation. The photocatalytic reaction primarily occurs through four sequential steps: photoexcitation, water ionization, oxygen adsorption, and superoxide protonation. Upon exposure to light, the semiconductor photocatalyst generates electron-hole pairs (e^- in the conduction band and h^+ in the valence band). These charge carriers then migrate to the catalyst surface, where oxidation and reduction reactions occur, driving the degradation of pollutants. Photocatalytic degradation of Rhodamine B (RhB) using 3D-printed TiO_2 structures primarily proceeds through the generation of reactive oxygen species under UV light irradiation. The mechanism involves excitation of TiO_2 when exposed to light with energy equal to or greater than its band gap (~3.2 eV for anatase), producing electron-hole pairs as shown in reaction equations (8)–(12) [52]:

$$TiO_2 + h\nu\ (UV) \rightarrow TiO_2\ (e^- + h^+) \quad (8)$$

$$h^+ + H_2O \rightarrow OH^\bullet + H^+ \quad (9)$$

$$OH^{-}_{ad} + h^{+} \rightarrow OH_{ad} \quad (10)$$

$$TiO_2\ (e^{-}) + O_2 \rightarrow TiO_{2\ 1} + O_2^{\bullet -} \quad (11)$$

$$RhB + \left(OH^{\cdot}, OH_{ad}, O_2^{-} \text{ or } h^{+} \rightarrow \text{degradation intermediates} \rightarrow CO_2 + H_2O\right. \quad (12)$$

In structured 3D-printed systems, light scattering, surface area, and flow-through design significantly affect degradation performance. Surface-anatase coating on printed shapes enhances photocatalytic efficiency by promoting a high density of active sites and stable electron-hole separation.

Similarly, the honeycomb filter achieved 99 % degradation of RhB within 210 min. The UV–Vis absorbance spectra showed a consistent decline at 553.5 nm, confirming steady and effective photodegradation. The pseudo-first-order rate constant was 0.017 ± 0.001 min^{-1}, with a strong correlation coefficient (R^2 = 0.983), indicating reliable kinetic behavior. Compared to the grid design, the honeycomb structure exhibited enhanced photocatalytic performance, likely due to its higher surface-to-volume ratio and more uniform internal geometry, which facilitates improved light distribution and greater exposure of active catalytic sites to UV irradiation. The gyroid filter exhibited the highest photocatalytic efficiency, achieving 99 % RhB degradation in 200 min. Kinetic analysis revealed a rate constant of 0.013 ± 0.001 min^{-1} and a linear correlation (R^2 = 0.987), confirming superior catalytic activity. Table 4 summarizes the different structures' rate constants, correlation coefficients, degradation times, and final efficiencies.

This enhanced performance is directly linked to the gyroid's triply periodic minimal surface (TPMS) architecture, which offers a significantly higher surface area and interconnected porosity than the grid and honeycomb structures (as shown in Table 2). According to recent studies [53], such TPMS geometries improve photon capture by enabling multidirectional UV light scattering and enhancing mass transfer by reducing diffusion limitations, which are critical in promoting efficient photocatalytic reactions. Furthermore, the hierarchical porous network of the gyroid allows for prolonged residence time of dye molecules and continuous exposure of fresh active sites, sustaining degradation performance over extended cycles. The rate constant serves as a critical parameter to assess the efficiency of the photocatalyst; a higher k value reflects more rapid degradation of the dye. Thus, the obtained value confirms the enhanced photocatalytic activity of the anatase-coated TiO_2 structures, attributed to their increased surface area and the presence of the photo-catalytically active anatase phase. The gyroid structure, with its higher K value due to enhanced porosity and surface interaction, displayed the fastest degradation rate.

During photocatalytic degradation of Rhodamine B using TiO_2, a blue shift (≈10 nm) in the absorbance peak is observed. This shift occurs due to stepwise N-deethylation, where ethyl groups are removed from the dye molecule by ROS generated by TiO_2 under UV light. As the dye loses its ethyl groups and aromatic structure, its conjugation is reduced, leading to absorption at shorter wavelengths [54,55]. Fig. 11 (d) shows the normalized concentration (C/C_0) of the target pollutant as a function of time, indicating the progression of photocatalytic degradation under light exposure. Fig. 11 (e) presents the degradation efficiency, calculated after a fixed period, to compare the effectiveness of each structure. Fig. 11 (f) illustrates the degradation kinetics, highlighting the reaction rates and confirming the kinetic behavior, often evaluated using a pseudo-first-order model. Table 5 summarizes key parameters of materials and printing methods used in photocatalytic applications, including dye type, initial concentration, degradation efficiency, time, rate constant, and references. It highlights how material composition and fabrication techniques affect photocatalytic performance in previous and present work.

3.6. Reusability of TiO_2 filter

To evaluate the stability of the TiO_2 photocatalyst, a reusability test was conducted using Rhodamine B under UV light at optimized conditions. The gyroid filters were reintroduced into 20 mL of Rhodamine B (12 ppm) contaminated water, and the photocatalytic performance remained consistent. UV irradiation was applied at hourly intervals, and the results demonstrated reproducibility. After 4 h of exposure, approximately 99 % degradation was achieved, as shown in Fig. 12.

Fig. 12 (a) shows the complete degradation of Rhodamine B within 240 min, while Fig. 12 (b) presents the kinetic performance of the gyroid sample after repeated use. The rate constant (k) of the reusable gyroid sample was determined to be 0.00376 min^{-1}, demonstrating that the photocatalyst retains significant activity even after multiple uses. While a slight reduction in efficiency is observed, potentially due to surface fouling or minor structural changes, the gyroid structure continues to effectively facilitate photocatalytic degradation, highlighting its promising reusability and durability for practical applications [60].

4. Conclusion

This study successfully demonstrates the fabrication of complex 3D-printed TiO_2 filters with grid, honeycomb, and gyroid geometries using DIW. An optimized ink formulation with 45 vol% TiO_2 was optimized to ensure printability, and photo initiator BAPO (1 wt% of the PEGDA) was found sufficient for curing the printed TiO_2 layers during the DIW process. The PEGDA-based photo-curable system (70 vol% PEGDA and 30 vol% PEG) facilitated excellent shape retention during the layer-wise deposition. The successful realization of these intricate designs, particularly the complex Gyroid TPMS structure, was enabled by an optimized ink rheology characterized by shear-thinning behavior and non-Newtonian flow ($n < 1$), enabling smooth extrusion and high structural fidelity post-extrusion. Binder removal at 600 °C followed by sintering at 1350 °C achieved a relative density of 92.19–94.81 %, indicating excellent densification and mechanical integrity suitable for photocatalytic applications. Grain growth was observed during sintering, with average particle size increasing from 600 nm to 1–1.2 μm. This growth is associated with the densification of the TiO_2 sample, indicating enhanced diffusion and microstructural evolution. XRD, SEM and EDS analyses confirmed the formation of the sol-gel-derived anatase uniform coating with a thickness of 4.3–4.5 μm on all geometries of TiO_2 filters, significantly enhancing the photocatalytic activity under UV irradiation.

The geometric architecture proved to be the dominant factor in photocatalytic performance. Among the structures tested, the gyroid geometry exhibited the highest performance, completely degrading Rhodamine B in 200 min. The honeycomb and grid structures also showed strong performance, achieving complete degradation in 210 and 330 min, respectively. The superior performance of the gyroid design is attributed to its intrinsic TPMS architecture, which provides the largest calculated surface area, along with optimized fluid dynamics and light-scattering properties. Further testing with methylene blue demonstrated

Table 4
Summarizes the rate constants, correlation coefficients, degradation times, and final degradation efficiencies for the different structures.

Structure	Rate Constant k (min^{-1})	Correlation Coefficient R^2	Time to Max. Degradation (min)	Degradation Efficiency (%)	Comment
Grid	0.0077 ± 0.0004	0.986	330	99	Slow
Honeycomb	0.017 ± 0.001	0.987	210	99	Moderate
Gyroid	0.013 ± 0.001	0.983	200	99	Fast

Table 5
Comparison of TiO_2 photocatalytic performance of 3D-printed materials and their degradation efficiency (FFT- Fused Filament Fabrication, DLP- Digital Light Processing).

Material and printing principle	Dye	C (ppm)	Degradation efficiency (%)	Degradation time (h)	K (min^{-1})	Ref
TiO_2 (FFF)	MB	1	–	–	0.0143	[56]
TiO_2(FFF)	MO	3	100	24	0.000067	[57]
TiO_2 (FFF)	MO	3	80	1.7	0.0375	[58]
TiO_2/Ag/Cu VP (DLP)	RhB	1000	99	1.3	–	[58]
TiO_2 (DLP)	MB	7	99	9	0.0066	[59]
TiO_2 (DIW)	RhB	12	99	5	0.011	Present work
	RhB	12	99	3.5	0.018	
	RhB	12	99	3.2	0.019	

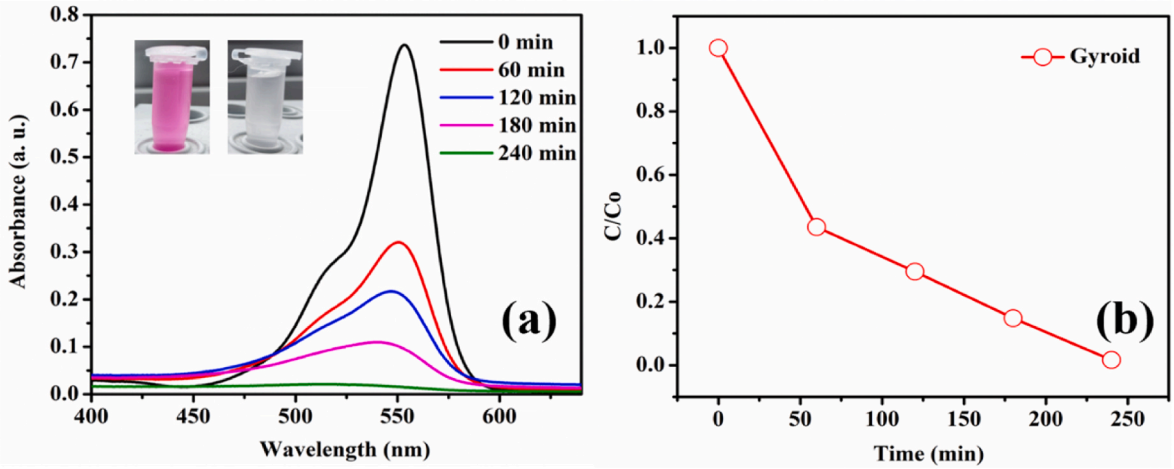

Fig. 12. (a) Reusability of the gyroid sample for the second cycle (b) Kinetics of the gyroid sample.

broad-spectrum photocatalytic activity, with complete degradation within 6 h. Overall, these results highlight the strong potential of geometry-optimized, surface-engineered TiO_2 filters for high-performance environmental remediation applications.

CRediT authorship contribution statement

Jyoti: Writing – review & editing, Writing – original draft, Validation, Methodology, Investigation, Formal analysis, Data curation, Conceptualization. **Marco Mariani:** Investigation. **Francesca Nanni:** Writing – review & editing, Supervision, Funding acquisition. **Claudia Mazzuca:** Writing – review & editing, Supervision, Investigation. **Mario Bragaglia:** Writing – review & editing, Supervision, Funding acquisition, Conceptualization.

Declaration of competing interest

We wish to declare that there are no known conflicts of interests or personal relationships that could have appeared to influence the work reported in this paper.

Appendix A. Supplementary data

Supplementary data to this article can be found online at https://doi.org/10.1016/j.ceramint.2025.11.372.

Data availability

Any data used in this paper is available from the authors upon request.

References

[1] T. Parangi, M.K. Mishra, Titania nanoparticles as modified photocatalysts: a review on design and development, Comments Inorg Chem 39 (2019) 90–126, https://doi.org/10.1080/02603594.2019.1592751.
[2] M. Bragaglia, M. Natali, D. Puglia, et al., Mechanical properties and infrared reflectance of TiO_2-Rubber compounds for cool-roof application, J. Appl. Polym. Sci. 142 (2025) 1–13, https://doi.org/10.1002/app.57244.
[3] K. Yaemsunthorn, M. Kobielusz, W. Macyk, TiO_2 with tunable anatase-to-rutile nanoparticles ratios: how does the photoactivity depend on the phase composition and the nature of photocatalytic reaction? ACS Appl. Nano Mater. 4 (2021) 633–643, https://doi.org/10.1021/acsanm.0c02932.
[4] M. Soleimani, J.B. Ghasemi, G. Mohammadi Ziarani, et al., Photocatalytic degradation of organic pollutants, viral and bacterial pathogens using titania nanoparticles, Inorg. Chem. Commun. 130 (2021) 108688, https://doi.org/10.1016/j.inoche.2021.108688.
[5] J. Carbajo, M. Jiménez, S. Miralles, et al., Study of application of titania catalysts on solar photocatalysis: influence of type of pollutants and water matrices, Chem Eng J 291 (2016) 64–73, https://doi.org/10.1016/j.cej.2016.01.092.
[6] A.H. Mamaghani, F. Haghighat, C.S. Lee, Effect of titanium dioxide properties and support material on photocatalytic oxidation of indoor air pollutants, Build. Environ. 189 (2021) 107518, https://doi.org/10.1016/j.buildenv.2020.107518.
[7] V. Seiß, S. Thiel, M. Eichelbaum, Preparation and real world applications of titania composite materials for photocatalytic surface, air, and water purification: state of the art, Inorganics 10 (2022), https://doi.org/10.3390/inorganics10090139.
[8] N.T. Padmanabhan, H. John, Titanium dioxide based self-cleaning smart surfaces: a short review, J. Environ. Chem. Eng. 8 (2020) 104211, https://doi.org/10.1016/j.jece.2020.104211.
[9] Z. Jing, D. Guo, W. Wang, et al., Comparative study of titania nanoparticles and nanotubes as antibacterial agents, Solid State Sci. 13 (2011) 1797–1803, https://doi.org/10.1016/j.solidstatesciences.2011.07.010.
[10] A. Dolganov, M.T. Bishop, G.Z. Chen, D. Hu, Rheological study and printability investigation of titania inks for direct ink writing process, Ceram. Int. 47 (2021) 12020–12027, https://doi.org/10.1016/j.ceramint.2021.01.045.
[11] Y. Li, L. Li, B. Li, Direct ink writing of special-shaped structures based on TiO_2 inks, Mod. Phys. Lett. B 30 (2016) 1650212, https://doi.org/10.1142/S0217984916502122.
[12] I.S.O. Barbosa, Y.A. Manrique, D. Paiva, et al., Efficient photocatalytic reactors via 3D printing: SLA fabrication and TiO_2 hybrid materials, RSC Adv. 15 (2025) 2275–2286, https://doi.org/10.1039/d4ra07121b.

[13] J. Bonilla-Cruz, M.A. Ávila-López, F.E.L. Rodríguez, et al., 3D printable ceramic pastes design: correlating rheology & printability, J. Eur. Ceram. Soc. 42 (2022) 6033–6039, https://doi.org/10.1016/j.jeurceramsoc.2022.06.029.

[14] Ávila-López MA, Lara-Ceniceros TE, Longoria FE, et al Photodegradation of air and water contaminants using 3D-Printed TiO_2Nanoparticle scaffolds. ACS Appl. Nano Mater. https://doi.org/10.1021/acsanm.2c02498.

[15] A. Elkoro, I. Casanova, 3D printing of structured nanotitania catalysts: a novel binder-free and low-temperature chemical sintering method, 3D Print. Addit. Manuf. 5 (2018) 220–226, https://doi.org/10.1089/3dp.2017.0164.

[16] M.A. Ávila-López, J. Bonilla-Cruz, J. Méndez-Nonell, Lara-ceniceros TE strong and lightweight stereolithographically 3D-Printed polymer nanocomposites with low friction and high toughness, Polymers 14 (2022), https://doi.org/10.3390/polym14173628.

[17] D.A. Kozlov, S.A. Tikhonova, P.V. Evdokimov, et al., Stereolithography 3D printing from suspensions containing titanium dioxide, Russ. J. Inorg. Chem. 65 (2020) 1958–1964, https://doi.org/10.1134/S0036023620120098.

[18] S. Mubarak, D. Dhamodharan, N. Divakaran, et al., Enhanced mechanical and thermal properties of stereolithography 3d printed structures by the effects of incorporated controllably annealed anatase TiO_2 nanoparticles, Nanomaterials 10 (2020), https://doi.org/10.3390/nano10010079.

[19] A. Vyatskikh, A. Kudo, S. Delalande, J.R. Greer, Additive manufacturing of polymer-derived titania for one-step solar water purification, Mater. Today Commun. 15 (2018) 288–293, https://doi.org/10.1016/j.mtcomm.2018.02.010.

[20] T. Chen, A. Sun, C. Chu, et al., Rheological behavior of titania ink and mechanical properties of titania ceramic structures by 3D direct ink writing using high solid loading titania ceramic ink, J. Alloys Compd. 783 (2019) 321–328, https://doi.org/10.1016/j.jallcom.2018.12.334.

[21] K. Lv, Q. Xiang, J. Yu, Effect of calcination temperature on morphology and photocatalytic activity of anatase TiO_2 nanosheets with exposed {001} facets, Appl. Catal. B Environ. 104 (2011) 275–281, https://doi.org/10.1016/j.apcatb.2011.03.019.

[22] S.P. Yasmeen, of B, NB, S.S. Tbmusstnuu, L. Burratti, L. Duranti, et al., Superior photodegradation of bentazon and nile blue and their binary mixture using sol–gel synthesized TiO_2 nanoparticles under UV and sunlight sources, Appl Sci 15 (2025), https://doi.org/10.3390/app15041899.

[23] P.J. Kelly, G.T. West, M. Ratova, et al., Structural formation and photocatalytic activity of magnetron sputtered titania and doped-titania coatings, Molecules 19 (2014) 16327–16348, https://doi.org/10.3390/molecules191016327.

[24] A. Kompa, D. Kekuda, K. Mohan Rao, A comparative study on the structural, optical, and electrical properties of titania films grown by spin-coating method, Appl. Phys. A Mater. Sci. Process. 126 (2020) 1–9, https://doi.org/10.1007/s00339-020-3405-z.

[25] D. Dastan, S.L. Panahi, N.B. Chaure, Characterization of titania thin films grown by dip-coating technique, J. Mater. Sci. Mater. Electron. 27 (2016) 12291–12296, https://doi.org/10.1007/s10854-016-4985-4.

[26] J. Swaminathan, S. Ravichandran, P. Palani, et al., Probing the defect-driven tunable photo(electro)catalytic water-splitting behavior of pulsed-laser-deposited titania, Energy Fuels 35 (2021) 4512–4523, https://doi.org/10.1021/acs.energyfuels.0c03784.

[27] J.L. Hodgkinson, H.M. Yates, A. Walter, et al., Roll to roll atmospheric pressure plasma enhanced CVD of titania as a step towards the realisation of large area perovskite solar cell technology, J. Mater. Chem. C 6 (2018) 1988–1995, https://doi.org/10.1039/c8tc00110c.

[28] L. Razzaboni, M. Altomare, M. Pedeferri, et al., Hierarchical anodic TiO_2 nanostructures formed in ethylene Glycol/o-H3PO4 electrolytes for direct photocatalysis, Chemelectrochem 7 (2020) 2859–2863, https://doi.org/10.1002/celc.202000673.

[29] M. Hassanpour, H. Safardoust-Hojaghan, Salavati-niasari M degradation of methylene blue and Rhodamine B as water pollutants via green synthesized Co3O4/ZnO nanocomposite, J. Mol. Liq. 229 (2017) 293–299, https://doi.org/10.1016/j.molliq.2016.12.090.

[30] R. Uma, K. Ravichandran, S. Sriram, Sakthivel B cost-effective fabrication of ZnO/g-C3N4 composite thin films for enhanced photocatalytic activity against three different dyes (MB, MG and RhB), Mater. Chem. Phys. 201 (2017) 147–155, https://doi.org/10.1016/j.matchemphys.2017.08.015.

[31] S. Rasalingam, R. Peng, Koodali RT an insight into the adsorption and photocatalytic degradation of rhodamine B in periodic mesoporous materials, Appl. Catal. B Environ. 174–175 (2015) 49–59, https://doi.org/10.1016/j.apcatb.2015.02.040.

[32] H.C. Vasconcelos, H. Carrêlo, T. Eleutério, et al., Rheology of cellulosic microfiber suspensions under oscillatory and rotational shear for biocomposite applications, Compounds 4 (2024) 688–707, https://doi.org/10.3390/compounds4040042.

[33] M.R. Kamal, V. Khoshkava, Effect of cellulose nanocrystals (CNC) on rheological and mechanical properties and crystallization behavior of PLA/CNC nanocomposites, Carbohydr. Polym. 123 (2015) 105–114, https://doi.org/10.1016/j.carbpol.2015.01.012.

[34] M.D. Chadwick, J.W. Goodwin, B. Vincent, et al., Rheological behaviour of titanium dioxide (uncoated anatase) in ethylene glycol, Colloids Surfaces A Physicochem Eng Asp 196 (2002) 235–245, https://doi.org/10.1016/S0927-7757(01)00898-6.

[35] Y. El Bitouri, N. Azéma, On the "Thixotropic" behavior of fresh cement pastes, Eng 3 (2022) 677–692, https://doi.org/10.3390/eng3040046.

[36] Gardini D, Backman L, Kaczmarek P, et al Viable Route to the Manufacture of Short Carbon fiber-rich UHTC Complex Shapes with Enhanced Toughness. Elsevier Ltd.

[37] R. Bernasconi, U. Bellè, S. Brigatti, M.V. Diamanti, 3D printing of photocatalytic nanocomposites containing titania nanoparticles, Addit. Manuf. 79 (2024), https://doi.org/10.1016/j.addma.2023.103916.

[38] N. Jamarun, D. Amelia, Rahmayeni, et al., The effect of temperature on the synthesis and characterization of hydroxyapatite-polyethylene glycol composites by in-situ process, Hybrid Adv. 2 (2023) 100031, https://doi.org/10.1016/j.hybadv.2023.100031.

[39] Pramono E. Khairuddin, S.B. Utomo, et al., FTIR studies on the effect of concentration of polyethylene glycol on polimerization of shellac, J Phys Conf Ser 776 (2016), https://doi.org/10.1088/1742-6596/776/1/012053.

[40] E. Wang, A. Hasheminasab, Y. Guo, et al., Structure characterization of UV-curing PEG-b-PPG-b-PEG dimethacrylate cross-linked network, Polymer (Guildf.) 153 (2018) 241–249, https://doi.org/10.1016/j.polymer.2018.02.040.

[41] T. Balaganapathi, B. Kaniamuthan, S. Vinoth, P. Thilakan, PEG assisted synthesis of porous TiO_2 using sol-gel processing and its characterization studies, Mater. Chem. Phys. 189 (2017) 50–55, https://doi.org/10.1016/j.matchemphys.2016.12.016.

[42] H. Budharaju, S. Suresh, M.P. Sekar, et al., Ceramic materials for 3D printing of biomimetic bone scaffolds – current state-of-the-art & future perspectives, Mater. Des. 231 (2023) 112064, https://doi.org/10.1016/j.matdes.2023.112064.

[43] A.E. Freitas, T.M. Manhabosco, R.J.C. Batista, et al., Development and characterization of titanium dioxide ceramic substrates with high dielectric permittivities, Materials 13 (2020), https://doi.org/10.3390/ma13020386.

[44] L.O. Grant, C.F. Higgs, Cordero ZC sintering mechanics of binder jet 3D printed ceramics treated with a reactive binder, J. Eur. Ceram. Soc. 43 (2023) 2601–2613, https://doi.org/10.1016/j.jeurceramsoc.2022.12.017.

[45] N.S. Mehta, S. Dey, V. Singh, M.R. Majhi, Analysis the effect of TiO_2 addition on sintering, physical mechanical behavior of porcelain insulating material, Appl. Surf. Sci. Adv. 4 (2021) 100083, https://doi.org/10.1016/j.apsadv.2021.100083.

[46] S. Chao, V. Petrovsky, F. Dogan, Effects of sintering temperature on the microstructure and dielectric properties of titanium dioxide ceramics, J. Mater. Sci. 45 (2010) 6685–6693, https://doi.org/10.1007/s10853-010-4761-4.

[47] A.H. Aleni, N. Kretzschmar, A. Jansson, et al., 3D printing of dense and porous TiO_2 structures, Ceram. Int. 46 (2020) 16725–16732, https://doi.org/10.1016/j.ceramint.2020.03.248.

[48] M.A. Caravaca, L.E. Kosteski, J.C. Miño, et al., Model for vickers microhardness prediction applied to SnO2 and TiO_2 in the normal and high pressure phases, J. Eur. Ceram. Soc. 34 (2014) 3791–3800, https://doi.org/10.1016/j.jeurceramsoc.2014.06.022.

[49] S. Haq, W. Rehman, M. Waseem, et al., Effect of heating on the structural and optical properties of TiO_2 nanoparticles: antibacterial activity, Appl. Nanosci. 8 (2018) 11–18, https://doi.org/10.1007/s13204-018-0647-6.

[50] H. Zhang, J.F. Banfield, Understanding polymorphic phase transformation behavior during growth of nanocrystalline aggregates: insights from TiO_2, J. Phys. Chem. B 104 (2000) 3481–3487, https://doi.org/10.1021/jp000499j.

[51] G. Li, Gray KA the solid-solid interface: explaining the high and unique photocatalytic reactivity of TiO_2-based nanocomposite materials, Chem. Phys. 339 (2007) 173–187, https://doi.org/10.1016/j.chemphys.2007.05.023.

[52] B. Kaur, P. Singh, S. Thakur, et al., Harnessing 3D printing for tailored TiO_2 structures redefining organic pollutant degradation, J. Environ. Chem. Eng. 13 (2025) 116042, https://doi.org/10.1016/j.jece.2025.116042.

[53] J. Feng, J. Fu, X. Yao, Y. He, Triply periodic minimal surface (TPMS) porous structures: from multi-scale design, precise additive manufacturing to multidisciplinary applications, Int. J. Extrem. Manuf. 4 (2022), https://doi.org/10.1088/2631-7990/ac5be6.

[54] S.Y. Lee, D. Kang, S. Jeong, et al., Photocatalytic degradation of rhodamine B dye by TiO_2 and gold nanoparticles supported on a floating porous polydimethylsiloxane sponge under ultraviolet and visible light irradiation, ACS Omega 5 (2020) 4233–4241, https://doi.org/10.1021/acsomega.9b04127.

[55] F. Sabatini, R. Giugliano, I. Degano, Photo-oxidation processes of Rhodamine B: a chromatographic and mass spectrometric approach, Microchem. J. 140 (2018) 114–122, https://doi.org/10.1016/j.microc.2018.04.018.

[56] A.J. Kennedy, A.D. McQueen, M.L. Ballentine, et al., Degradation of microcystin algal toxin by 3D printable polymer immobilized photocatalytic TiO_2, Chem Eng J 455 (2023) 140866, https://doi.org/10.1016/j.cej.2022.140866.

[57] A. Sangiorgi, Z. Gonzalez, A. Ferrandez-Montero, et al., Printing of photocatalytic filters using a biopolymer to immobilize TiO_2 nanoparticles, J. Electrochem. Soc. 166 (2019) H3239–H3248, https://doi.org/10.1149/2.0341905jes.

[58] W. Huang, H. Mei, P. Chang, et al., Tailoring soft-flexible negative Poisson's ratio support to boost photocatalytic efficiency: from dissociation to anchoring, Addit. Manuf. 58 (2022) 103059, https://doi.org/10.1016/j.addma.2022.103059.

[59] C.H. Chen, S.C. Wang, H.W. Chen, et al., High-efficiency photocatalytic reactors fabricated via rapid DLP 3D printing: enhanced dye photodegradation with optimized TiO_2 loading and structural design, ACS ES&T Water 4 (2024) 1883–1893, https://doi.org/10.1021/acsestwater.4c00002.

[60] Q. Sun, K. Li, S. Wu, et al., Remarkable improvement of TiO_2 for dye photocatalytic degradation by a facile post-treatment, New J. Chem. 44 (2020) 1942–1952, https://doi.org/10.1039/c9nj05120a.